

Perspectives and limitations of symmetric X-ray Bragg reflections for inspecting polytypism in nanowires

Martin Köhl,^{a*} Philipp Schroth^a and Tilo Baumbach^{a,b,c}

Received 24 September 2015

Accepted 7 January 2016

Edited by V. Favre-Nicolin, CEA and Université Joseph Fourier, France

Keywords: diffraction; nanowires; GaAs; polytypism.

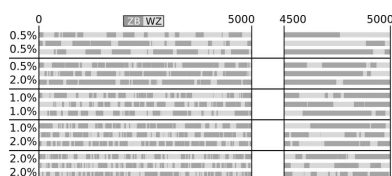
^aInstitute for Photon Science and Synchrotron Radiation, Karlsruhe Institute of Technology, Hermann-von-Helmholtz-Platz 1, 76344 Eggenstein-Leopoldshafen, Germany, ^bANKA, Karlsruhe Institute of Technology, Hermann-von-Helmholtz-Platz 1, 76344 Eggenstein-Leopoldshafen, Germany, and ^cLaboratory for Application of Synchrotron Radiation, Karlsruhe Institute of Technology, Kaiserstrasse 12, 76131 Karlsruhe, Germany. *Correspondence e-mail: martin.koehl@kit.edu

X-ray diffraction, possibly time-resolved during growth or annealing, is an important technique for the investigation of polytypism in free-standing nanowires. A major advantage of the X-ray diffraction approach for adequately chosen beam conditions is its high statistical significance in comparison with transmission electron microscopy. In this manuscript the interpretation of such X-ray intensity distribution is discussed, and is shown to be non-trivial and non-unique given measurements of the $[111]_c$ or $[333]_c$ reflection of polytypic nanowires grown in the $(111)_c$ direction. In particular, the diffracted intensity distributions for several statistical distributions of the polytypes inside the nanowires are simulated and compared. As an example, polytypic GaAs nanowires are employed, grown on a Si-(111) substrate with an interplanar spacing of the Ga (or As) planes in the wurtzite arrangement that is 0.7% larger than in the zinc blende arrangement along the $(111)_c$ direction. Most importantly, ambiguities of high experimental relevance in the case of strongly fluctuating length of the defect-free polytype segments in the nanowires are demonstrated. As a consequence of these ambiguities, a large set of deviations from the widely used Markov model for the stacking sequences of the nanowires cannot be detected in the X-ray diffraction data. Thus, the results here are of high relevance for the proper interpretation of such data.

1. Introduction

The formation of microstructures and nanostructures is a complicated microscopic process. In order to improve the understanding of the involved dynamical processes during growth, time-resolved *in situ* investigations during the growth proved highly valuable in many cases. Nowadays, adequate instrumentation capable of performing various well established post-growth *ex situ* methods time-resolved and *in situ* is available, ranging from environmental transmission electron microscopy (eTEM) (Moseler *et al.*, 2010; Gamalski *et al.*, 2011, 2012; Zheng *et al.*, 2013) to growth chambers suited for time-resolved *in situ* X-ray investigations during sputtering (Kaufholz *et al.*, 2015) or molecular beam epitaxy (Schroth *et al.*, 2012, 2015; Biermanns *et al.*, 2014; Krogstrup *et al.*, 2012; Slobodskyy *et al.*, 2012).

Nevertheless, such time-resolved *in situ* measurements are still challenging. Typically, restrictions of the *in situ* instrumentation, compared with respective *ex situ* measurements, must be taken into account. In the case of X-ray investigations, three restrictions of high relevance are: (i) geometrical limitations which stem from the size and position of the incidence and exit windows of the growth environment for the



X-ray beam, (ii) limitations in the flexibility and precision in moving the sample (inside the growth chamber or the growth chamber itself) and (iii) the incident X-ray flux. Despite these challenges, time-resolved *in situ* X-ray measurements of the $[111]_c$ reflection of strongly polytypic GaAs nanowires have been performed and evaluated in the framework of a Markov model (Schroth *et al.*, 2015). The index in our notation for Bragg reflections (such as $[111]_c$) and crystallographic directions indicates whether the given numbers are based on a cubic crystallographic basis (index c) or a hexagonal crystallographic basis (index h). More details are given in §2.3 [see, in particular, equation (17)].

Although the focus of this manuscript is the investigation of the wurtzite zinc blende polytypism by measuring the $[hhh]_c$ reflections ($h \in \mathbb{N}$), we emphasize that many other aspects of nanowire growth can be studied by time-resolved *in situ* X-ray diffraction experiments [*e.g.* scaling laws linking radial and axial nanowire growth (Dubrovskii *et al.*, 2012) by employing the Plancherel theorem].

We point out that such X-ray diffraction measurements are complementary to transmission electron microscopy investigations (TEM) of polytypism (Johansson *et al.*, 2006; Moseler *et al.*, 2010; Gamalski *et al.*, 2011, 2012): whereas the latter produces direct space images of a limited field of view for a low number of wires up to atomic resolution, X-ray diffraction is a probe of reciprocal space and best suited for investigation of a large ensemble of nanowires [although measurements of single wires can also be made (Biermanns *et al.*, 2009; Biermanns, 2012)].

Polytypism refers to the observation that multiple crystalline atomic arrangements of the constituting atoms can be observed even in a single nanowire [see, for example, Caroff *et al.* (2011) for a short review]. The phenomenon has its origin in differences of the energetic barriers for nucleating either polytype comparable with thermal energy scale $k_B T_{\text{Growth}}$, where k_B is the Boltzmann constant and T_{Growth} is the growth temperature of the nanostructure (Johansson *et al.*, 2006, 2009; Glas *et al.*, 2007; Algra *et al.*, 2008). Polytypism can be found in various material systems (Dick *et al.*, 2010; Kriegner *et al.*, 2011) such as GaAs, InAs (Mandl *et al.*, 2006; Takahashi & Morizumi, 1966; Zheng *et al.*, 2013; Joyce *et al.*, 2010), InSb or InP (Algra *et al.*, 2008). Understanding and controlling this polytypism is particularly important for advancing applications of nanowires, since it deteriorates electronic and optical properties of III/V nanowires (Hjort *et al.*, 2013; Bao *et al.*, 2008; Spirkoska *et al.*, 2009; Heiss *et al.*, 2011; Cahangirov & Ciraci, 2009).

Typically, in addition to the structure of the crystalline building blocks, a small change in the inter-atomic distances is observed (Yeh *et al.*, 1992; Panse *et al.*, 2011; Biermanns *et al.*, 2011; Biermanns, 2012; Tchernycheva *et al.*, 2006; Mariager *et al.*, 2010). In the case of GaAs nanowires grown in the cubic $(111)_c$ direction, zinc blende as well as wurtzite segments can be observed (Johansson *et al.*, 2012; Schroth *et al.*, 2015; Biermanns, 2012). The ratio of their inter-layer spacings d_{wz} in the $(00.2)_h$ direction and d_{zb} in the $(111)_c$ direction is

approximately $d_{wz}/d_{zb} \simeq 1 + 0.7\%$ (Köhl *et al.*, 2015; Biermanns *et al.*, 2011; Biermanns, 2012).

Both aspects, *i.e.* the differences in the inter-planar spacings as well as the distinct crystallographic symmetries of the polytypes, are means to investigating polytypic nanowires with X-ray diffraction. However, discriminating the polytypes by their symmetry requires measurements of multiple reflections either in non-coplanar or asymmetric geometry (or a combination thereof) and, thus, are more challenging in the case of time-resolved *in situ* X-ray investigations due to the above-mentioned restrictions (i)–(iii). Nonetheless, very sophisticated modelling of the scattering of polytypic crystals with non-zero in-plane momentum transfer (*e.g.* the series $[10.L]_h$ of reflections) has already been carried out (see, for example, Sebastian & Krishna, 1987). Contrarily, measurements of the $[111]_c$ reflection are comparably easy to realise experimentally, but this reflection only discriminates the polytypes by their slightly different lattice constants and not by their symmetry. As a consequence, zinc blende and its twin structure are indistinguishable.

Nonetheless, a deep understanding of the perspectives and limitations of measurements of the $[111]_c$ reflection is one very important aspect for planning and evaluation of experiments with polytypic nanowires. In this manuscript, we discuss these aspects for measurements of an ensemble of nanowires for conditions where the coherence of the X-ray beam results in interference from a single or few wires, but a very large number of such coherence volumes is illuminated simultaneously. Based on extensive numerical simulations, we address the challenge of proper interpretation of such diffraction data: how do characteristic features in the distribution of the polytype segments in the nanowires influence the ensemble averaged diffraction signal? Which statistical properties of the polytype segment distribution are indistinguishable? Can we detect the occurrence of higher-order polytypes (such as the $4H$ polytype) beyond their statistically expected occurrence (Johansson *et al.*, 2012)? In addition, we discuss the relation between the cubic $[333]_c$ and $[111]_c$ reflection.

We do neither discuss the separation of the scattering from the nanowires and parasitic growth (Köhl *et al.*, 2015) nor data evaluation of single-nanowire X-ray measurements (Biermanns *et al.*, 2009; Biermanns, 2012; Köhl *et al.*, 2012, 2013; Minkevich *et al.*, 2014; Rodriguez *et al.*, 2013; Marchesini, 2007*a,b*; Adams *et al.*, 2012; Chushkin & Zontone, 2013; Trahan & Hyland, 2013) in this manuscript.

Our reference case is the Markov model for the stacking in the nanowires, since this model is compatible with high-resolution transmission electron microscopy (HRTEM) by Johansson *et al.* for highly faulty polytypic nanowires (exponential distribution for the faultless phase segment length distribution with an average defect-free segment thickness of the order of three to nine layers) (Johansson *et al.*, 2006, 2009) and recent time-resolved *in situ* X-ray investigations (Schroth *et al.*, 2015) with average defect-free segment thicknesses of the order of 50–400 layers. Therefore, we also provide an extended discussion of the Markov model, including the

influence of initial growth and the X-ray scattering within this model in this manuscript.

The focus of our manuscript is transition probabilities from one polytype to the other less than 5% per grown layer. Since most applications aim for nanowires with high phase purity (*i.e.* low transition probabilities), this range of transition probabilities is of high practical relevance. For larger transition probabilities, more sophisticated modelling of the lattice spacings inside the nanowires is needed (incorporation of strain close to the interfaces between the different polytypes), but this range can also be studied well with TEM even on a statistical level.

2. Theoretical background

For simulations of the X-ray diffraction signal close to a $[hhh]_c$ ($h \in \mathbb{N}$) reflection, we must define: (1) a model for the geometry of the nanowires. The geometry includes parameters such as the height (distribution), diameter (distribution) and tapering (*i.e.* a change of the diameter of the nanowire along its axial growth direction); (2) a model for the stacking sequence of the atomic planes in the axial growth direction; and, finally, (3) a model for the X-ray scattering of those structures.

Throughout the manuscript, we assume that the geometrical information on the nanowires is available (*e.g.* from post-growth *ex situ* measurements) and limit our discussion to the extraction of information about stacking sequence for given geometric information. Moreover, we neglect parasitic growth and focus on the diffraction from the polytypic nanowires only.

We now discuss two approaches for modelling the stacking sequence of the nanowires (see Fig. 1) before we turn to point (3) from above.

On the one hand, we employ a single GaAs layer as the fundamental building block in the construction of the stacking sequences in our ensemble of nanowires. In that case, a limited history of previous layers in the stacking sequence determines the probabilities p_{ZB} and $p_{WZ} = 1 - p_{ZB}$ for the newly grown layer to constitute a zinc blende or wurtzite stacking, respectively. This ‘layer-by-layer’ approach is a Markovian model.

On the other hand, we employ a faultless segment of either polytype as a fundamental building block in the construction of the stacking (‘segment-by-segment’ growth). Here, the length of such a building block is taken from various random distributions.

Whereas the Markov model is particularly useful if a very limited number of previous layers of the crystalline structure dominates the growth of new layer, the second model is more appropriate if the growth dynamics cannot be reduced to a very limited history in the crystalline structure. For such conditions, the number of free parameters in a high-order Markovian model is too high to be of practical use. The two approaches are, however, connected by the exponential distribution [see Fig. 1 and equation (2)].

Along the $(111)_c$ direction, every layer j of height d_j consists of a plane of arsenic atoms at $z = 0$ and gallium atoms at $z = 0.75d_j$. The arrangement perpendicular to this $(111)_c$ direction

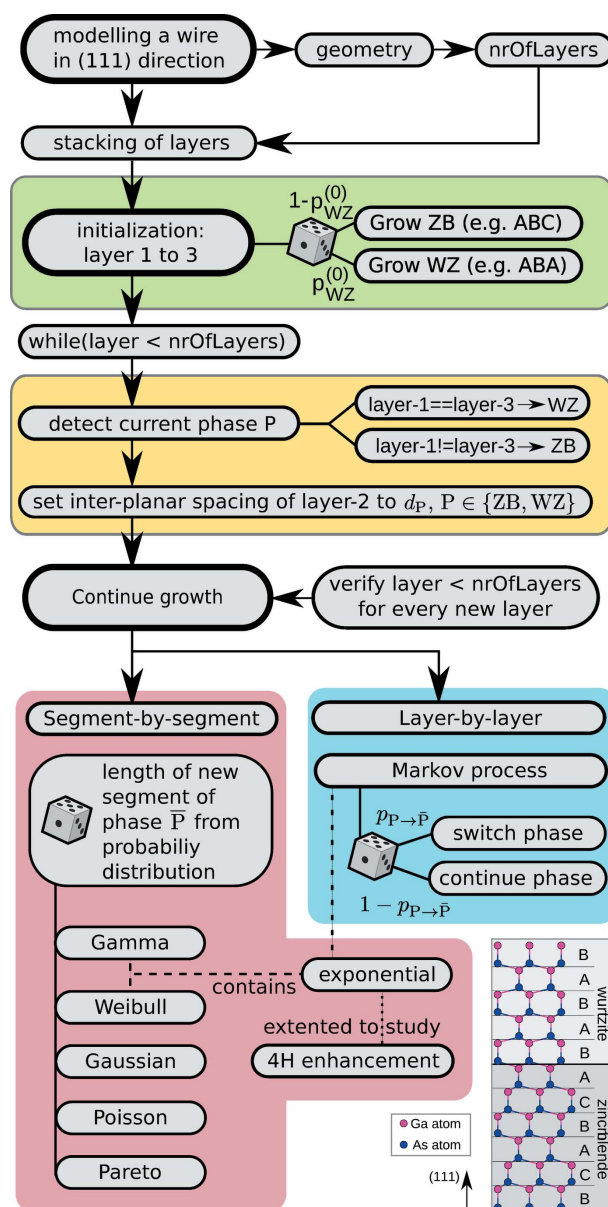


Figure 1
Schematic overview of our simulations.

determines the stacking (see Fig. 1): if only two alternating positions $\mathbf{x}_\perp \perp \hat{\mathbf{e}}_{(111)_c} \equiv \hat{\mathbf{e}}_z$ repeat periodically, we have the wurtzite stacking (*e.g.* $ABAB \dots$). If three alternating positions $\mathbf{x}_\perp \perp \hat{\mathbf{e}}_z$ repeat periodically, we end up with a zinc blende structure (*e.g.* $ABCABC \dots$). Twinned zinc blende permutes the composition in this fundamental unit and refers to the permutation $ACBACB \dots$ if the non-twinned structure is given by $ABCABC \dots$. The before-mentioned *4H* polytype refers to a periodic repetition of wurtzite and zinc blende, *i.e.* $ABCBACB \dots$. For an introduction to other higher-order polytypes, we refer the reader to Johansson *et al.* (2012) where an overview is given.

For the detection of the current phase, the history of the previous three layers is required if we restrict to the zinc blende and wurtzite polytype. If the layers $j - 1$ and $j - 3$ are of equal type, the current phase (‘local phase’) is wurtzite. If

those layers are of different type, the local phase is zinc blende.

Irrespective of the growth dynamics for layers $j \gg 1$, we summarize the initial nucleation stage in a single parameter $p_{\text{WZ}}^{(0)} = 1 - p_{\text{ZB}}^{(0)}$ which describes the probability for beginning the stacking as a wurtzite segment.

Moreover, we approximate the number of layers N_L in the nanowire by its geometric height divided by the approximate layer spacing $d_j \approx a_{(111)_c} \simeq 3.26 \text{ \AA}$ where $a_{(111)_c}$ is the distance in the cubic $(111)_c$ direction in bulk zinc blende GaAs. Once this number of layers N_L is reached, the generation of the stacking sequence of a nanowire is finished.

2.1. Layer-by-layer modelling of the stacking (Markov model)

We now discuss the layer-by-layer approach in detail. In the lowest-order Markov model, we restrict to the history of exactly three layers. Fewer layers are insufficient for distinguishing the two polytypes, whereas the number of free parameters grows rapidly with each additional layer that is considered in the history. In this Markov model, the two independent parameters $p_{\text{P|P}}$ parametrize the probability for continuing growth of the current polytype $\text{P} \in \{\text{ZB}, \text{WZ}\}$. The probabilities for switching the current polytype to the complementary polytype $\bar{\text{P}}$ are consequently given by $p_{\bar{\text{P}}|\text{P}} = 1 - p_{\text{P|P}}$ ('transition probabilities').

Suppose layer $m - 1$ is of polytype $\bar{\text{P}}$ and layer m of polytype P : then, the probability for this segment starting at layer m to continue $n \geq 1$ layers in the stacking of polytype P and switch back to polytype $\bar{\text{P}}$ at layer $m + n$ is

$$p_{\text{P}}^{(\text{loc})}(n, m) = \mathcal{N}_m \left[\prod_{k=2}^n p_{\text{P|P}}(m+k-2) \right] p_{\bar{\text{P}}|\text{P}}(m+n-1), \quad (1)$$

where \mathcal{N}_m is the normalization of the probability distribution for every layer m where a new segment begins. For $n = 1$, we define $\prod_{k=2}^n \dots = 1$. If the probabilities $p_{\text{P|P}}$ are independent of the current layer, the probability $p_{\text{P}}^{(\text{loc})}(n, m)$ simplifies to the exponential distribution

$$p_{\text{P}}^{(\text{loc})}(n) = \frac{\exp(-n/b_{\text{P}})}{b_{\text{P}}}, \quad (2)$$

with the decay length

$$b_{\text{P}} = \frac{-1}{\log(p_{\text{P|P}})} = \frac{-1}{\log(1 - p_{\bar{\text{P}}|\text{P}})} \stackrel{p_{\bar{\text{P}}|\text{P}} \ll 1}{\approx} \frac{1}{p_{\bar{\text{P}}|\text{P}}}. \quad (3)$$

The interpretation of equation (1), where n is integer valued, as an exponential distribution with continuous real valued parameter n is valid if and only if $b_{\text{P}} \gg 1$ which is equivalent to $p_{\bar{\text{P}}|\text{P}} \ll 1$. Therefore, the approximation in equation (3) is valid.

In Fig. 2, some typical polytype distributions inside nanowires are depicted for various values for $p_{\bar{\text{P}}|\text{P}}$ for illustration (see also Schroth *et al.*, 2015).

If we incorporate the initial growth $p_{\text{P}}^{(0)}$ for the layers $j = 1, 2, 3$, we are able to recursively calculate the probability $q_{\text{P}}(j)$ of layer j in an ensemble of nanowires to be of polytype P from

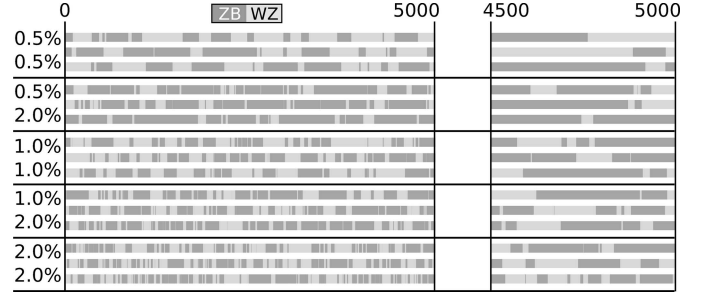


Figure 2

Illustrations of polytype distribution inside nanowires generated according to the Markov model discussed in the main text. The upper parameter value refers to $p_{\text{WZ|ZB}}$, the lower value to $p_{\text{ZB|WZ}}$, and $p_{\text{P}}^{(0)}$ was set to 0.5%. The layers $j = 0-5000$ have been depicted. Moreover, the range $j = 4500-5000$ has been magnified.

$$q_{\text{P}}(j) \stackrel{j \leq 3}{=} p_{\text{P}}^{(0)}, \quad (4a)$$

$$q_{\text{P}}(j) \stackrel{j > 3}{=} q_{\text{P}}(j-1)p_{\text{P|P}}(j-1) + q_{\bar{\text{P}}}(j-1)p_{\bar{\text{P}}|\text{P}}(j-1). \quad (4b)$$

If we define

$$\tilde{p}_{\text{S}}(j) = 1 - \sum_{\text{P} \in \{\text{ZB}, \text{WZ}\}} p_{\text{P|P}}(j) \quad (5)$$

and exploit that for every layer j we have $q_{\text{P}} + q_{\bar{\text{P}}} = 1$ and $p_{\text{P|P}} = 1 - p_{\bar{\text{P}}|\text{P}}$, the recursive definition simplifies to

$$q_{\text{P}}(j) \stackrel{j > 3}{=} q_{\text{P}}(j-1)\tilde{p}_{\text{S}}(j-1) + p_{\bar{\text{P}}|\text{P}}(j-1). \quad (6)$$

If the transition probabilities $p_{\bar{\text{P}}|\text{P}}$ are layer independent and the wires change their polytype during growth (*i.e.* $\tilde{p}_{\text{S}} < 1$), this recursive definition is equivalent to explicit formula

$$q_{\text{P}}(j) \stackrel{j > 3}{=} \tilde{p}_{\text{S}}^{j-3} p_{\text{P}}^{(0)} + (1 - \tilde{p}_{\text{S}}^{j-3}) \check{s}_{\text{P}}, \quad (7)$$

which represents a weighted average of the initial growth $p_{\text{P}}^{(0)}$ and the stationary limit for the probability of polytype P ,

$$\check{s}_{\text{P}} = \frac{p_{\bar{\text{P}}|\text{P}}}{1 - \tilde{p}_{\text{S}}} = \frac{1}{1 + (p_{\bar{\text{P}}|\text{P}}/p_{\text{P|P}})} \quad (8)$$

in the limit $j \rightarrow \infty$.

Consequently, a simultaneous rescaling $p_{\bar{\text{P}}|\text{P}} \rightarrow \alpha p_{\bar{\text{P}}|\text{P}}$, $\alpha \in \mathbb{R}$, for both polytypes P results in the same fractions \check{s}_{P} of each polytype in the stationary limit. However, the phase purities, which we define to be the expectation value of the distribution of lengths of the defect-free polytype segments, scale as $b_{\text{P}} \rightarrow \alpha^{-1} b_{\text{P}}$.

We point out that most applications require two properties of the phase-length distribution: a large mean value (*i.e.* on average long segments without stacking defects) and low fluctuations around this mean (low probability for short segments and in order to guarantee correlations in superlattice structures). Neither of these two requirements can be estimated solely from the phase fractions \check{s}_{P} . However, the phase fractions can be estimated if the phase purities are known.

As long as growth of the nanowires can be approximately described by such a low-order Markov model, the before-

mentioned fluctuations cannot be controlled separately from the mean value, since the standard deviation of the exponential distribution is equal to its mean value.

The weight \tilde{p}_s^{j-3} of $p_p^{(0)}$ in equation (7) drops below $\exp(-1)$ for

$$j > 3 + \frac{-1}{\log(\tilde{p}_s)} \stackrel{\tilde{p}_s \lesssim 1}{\approx} \frac{1}{\sum_P p_{P|\bar{P}}} = \frac{\prod_P b_P}{\sum_P b_P}. \quad (9)$$

Thus, we can estimate the ‘memory’ of the stacking sequences for the initial growth polytype probability $p_p^{(0)}$ in the Markov model. Given the values for b_p , it is therefore possible to decide whether the initial growth behaviour, the stationary growth limit or some mixture is observed in a particular growth experiment.

We would like to point out that X-ray measurements typically probe the entire nanowire volume and, thereby, only detect the average phase fractions

$$\check{m}_p(N_L) \stackrel{N_L \gg 2}{\equiv} \frac{1}{N_L} \sum_{j=1}^{N_L} q_p(j) \quad (10a)$$

$$= \left[\frac{3}{N_L} + \frac{\tilde{p}_s}{N_L} \left(\frac{1 - \tilde{p}_s^{j-3}}{1 - \tilde{p}_s} \right) \right] p_p^{(0)} + \left[\left(\frac{N_L - 3}{N_L} \right) - \frac{\tilde{p}_s}{N_L} \left(\frac{1 - \tilde{p}_s^{j-3}}{1 - \tilde{p}_s} \right) \right] \check{s}_p \quad (10b)$$

throughout the entire wire. This mean phase fraction is again expressed as a weighted average of $p_p^{(0)}$ and \check{s}_p for convenience. Moreover, $\check{m}_p(N_L) \stackrel{N_L \rightarrow \infty}{\equiv} \check{s}_p$ and $\check{m}_p(N_L) \stackrel{N_L=3}{\equiv} p_p^{(0)}$. The quantities q_p and \check{m}_p are depicted as a function of the currently growing layer j in Fig. 3. Therefore, it is possible to detect traces of the initial growth behaviour in X-ray experiments even if its influence is already negligible for the top-most layer N_L .

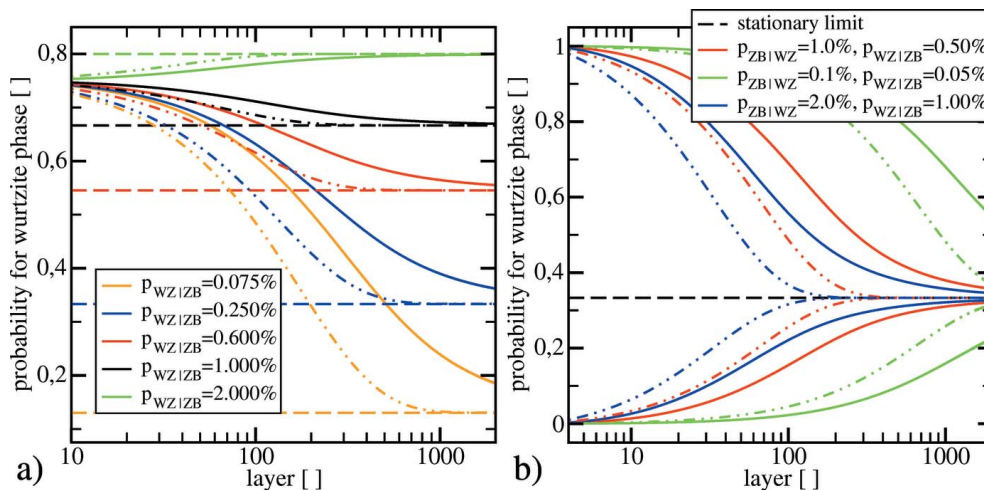


Figure 3

Influence of initial growth in the Markov model. The dashed-dotted lines illustrate q_p for wurtzite as a function of the currently growing layer j [see equation (7)], whereas the continuous lines refer to the mean phase fraction $\check{m}_p(j)$ from layer 1 up to the currently growing layer j [see equation (10b)]. The dashed black line shows the stationary limit for $j \rightarrow \infty$ [see equation (8)]. (a) Fixed value $p_p^{(0)} = 0.75$ for the initial growth and transition probability $p_{ZB|WZ} = 0.5\%$. (b) Fixed stationary limit \check{s}_p and extreme cases $p_p^{(0)}$ equal to 0 and 1.

2.2. Segment-by-segment modelling of the stacking sequence

We now turn to segment-by-segment growth for the nanowire stacking.

Instead of a single layer j , a segment of length $N_s \geq 1$ of the complementary polytype \bar{P} with respect to the previously grown polytype is added. This length N_s is drawn from a random distribution. The polytype of the initial segment is determined by the probabilities $p_p^{(0)}$.

If we consider exponential distributions [see equation (2)], the segment-by-segment approach is identical to the Markov model with constant transition probabilities. An important property of the exponential distribution is that it is a special case of both the Gamma distribution

$$\mathcal{G}(x, b, m) = \frac{1}{b \Gamma(m+1)} \left(\frac{x}{b} \right)^m \exp(-x/b) \quad (11)$$

as well as the Weibull distribution

$$\mathcal{W}(x, b, m) = \frac{1+m}{b} \left(\frac{x}{b} \right)^m \exp[-(x/b)^{1+m}] \quad (12)$$

if we set $m = 0$. The parameters N_s , b and m are constrained by $x \geq 0$, $m > -1$ and $b > 0$. Here, we suppressed the dependence of these parameters on the polytype for simplicity. We map $x > 0 \in \mathbb{R}$ to an integer value for the number of layers $N_s \geq 1$ by $N_s = \text{round}(x + 0.5)$.

If we compare these two distributions with the special case of the exponential distribution, the power-law x^m strongly influences the occurrence of short segments: for $m > 0$, the probability of short segments is strongly reduced as compared with the Markov model. For any $m > 0$, the maximum of the probability distribution is no longer located at $x = 0$. In contrast, for $m < 0$, the probability for short segments is enhanced and the probability distributions \mathcal{G} and \mathcal{W} diverge for $x \rightarrow 0^+$. However, by the constraint $m > -1$, the divergences are integrable as required for probability distributions.

The behaviour of long segments is dominated by the exponential terms in both distributions. In contrast to the Weibull distribution, the exponential term is not influenced by the parameter m in the Gamma distribution. For the Weibull distribution, $m > 0$ implies a faster decay of the probability for long segments than for the exponential distribution whereas $m < 0$ reduces this decay.

Consequently, the segment-by-segment modelling with Gamma and Weibull distributions is very useful for studying the influence of deviations from the Markov model on the X-ray diffraction signal, regardless of the microscopic origin of such deviations.

In order to understand the results obtained during this investigation, we also investigate (truncated) Gaussian distributions

$$S(x, \mu_S, \sigma_S) = \frac{\Theta(x)}{\sigma_S \sqrt{2\pi}} \exp\left[-\frac{1}{2} \left(\frac{x - \mu_S}{\sigma_S}\right)^2\right] \quad (13)$$

where we can tune the mean value μ_S and width σ_S independently. Here $\Theta(x)$ is the Heaviside step function.

Moreover, we also consider the Poisson distribution

$$\mathcal{R}(N_S, \lambda) = \frac{\lambda^{N_S-1}}{(N_S - 1)!} \exp(-\lambda). \quad (14)$$

Finally, it is interesting to observe the scattering signal of distributions which are not dominated by an exponential function for large segments $N_S \gg 1$. Consequently, we also include the Pareto distribution

$$\mathcal{P}(x, \gamma, m) = \frac{\gamma}{m} \left(\frac{m}{x+1}\right)^{\gamma+1}, \quad x \geq m - 1 \quad (15)$$

for $m = 1$ in our investigations. Therefore, we define $\mathcal{P}(x, \gamma) \equiv \mathcal{P}(x, \gamma, m = 1)$.

A summary of the statistical distributions that are relevant in this manuscript is given in Table 1.

We point out that, depending on the random distribution for N_S , the ‘memory’ of the stacking for its initial polytype, *i.e.*

$p_P^{(0)}$, may differ strongly from the ‘memory’ in the Markov model [see equations (7) and (10b)] if the stacking of the nanowires is generated according to the segment-by-segment model.

2.3. X-ray scattering of polytypic nanowires

We now discuss the X-ray scattering of polytypic nanowires once their stacking sequences as well as their geometry are known.

First, a single nanowire is small enough that multiple scattering in a single wire can be neglected and we restrict to a lowest-order Born approximation (‘kinematic approximation’). Moreover, for typical sample–detector distances of the order of 1 m, it is also valid to assume far-field conditions. Consequently, the scattering of a single wire can be approximated by the Fourier transform of the electron density,

$$\varrho_{\text{el}}(\mathbf{x}) = \sum_{j=1}^{N_L} \Omega^{(j)}(\mathbf{x}_{\perp}) \sum_{\alpha \in \{\text{Ga,As}\}} \varrho_{\text{el}}^{(j\alpha)}(\mathbf{x}_{\perp}, z), \quad (16)$$

where $\Omega^{(j)}(\mathbf{x}_{\perp})$ is the shape function of layer j and $\varrho_{\text{el}}^{(j\alpha)}(\mathbf{x}_{\perp}, z)$ is the electron density of sub-layer α in layer j . Here, z points in the cubic (111)_c or (001)_h direction. Here, we repeat that every layer j of height d_j consists of two atomic planes: a plane of arsenic atoms centred at $z = 0$ and a plane of gallium atoms centred around $z = 0.75d_j$.

In the subsequent discussions, we restrict to the vicinity of symmetric Bragg reflections

$$\mathbf{Q}_B = [hhh]_{z \rightarrow c} = [00.(3h)]_{z \rightarrow h1} \approx [00.(2h)]_{w \rightarrow h2}. \quad (17)$$

$[hhh]_{z \rightarrow c}$ refers to the Miller Bravais indices of a cubic lattice expressed in the conventional cubic unit cell, whereas $[00.(3h)]_{z \rightarrow h1}$ refers to the same reflection of a cubic lattice but expressed in hexagonal surface coordinates instead. In this coordinate system the zinc blende structure simplifies to a three-layer periodic stacking (such as *ABCABC...*) along the surface normal. If the length of the surface normal is normalized to this three-layer periodicity, the Bragg indices

$[hhh]_{z \rightarrow c} = [00.(3h)]_{z \rightarrow h1}$ refer to the same location in reciprocal space. If the surface normal of the hexagonal surface coordinate system is instead normalized to a hexagonal crystalline structure, which has the two-layer periodic wurtzite stacking (such as *ABAB...*) in the direction of the surface normal, the indices must be rescaled by a factor of 2/3. For this normalization, we employ the notation $[*]_{w \rightarrow h2}$. If the inter-planar distance of two successive layers, *e.g.* of type *A* and *B*, of the zinc blende and wurtzite structure

Table 1

Overview of statistical distributions used for the generation of phase segments of either zinc blende or wurtzite phase with random length.

Gamma and Weibull distributions reduce to an exponential distribution for $m = 0$. $\Gamma(\cdot)$ denotes the Gamma function. Gamma, Weibull, Pareto and Gaussian distributions are two-parameter distributions whereas the exponential and Poisson distribution are one-parameter distributions.

Distribution	Density function	Mean	Variance
Exponential	$\frac{\exp(-x/b_p)}{b_p}$	b_p	b_p^2
Gamma	$\frac{1}{b \Gamma(m+1)} (x/b)^m \exp(-x/b)$, $b > 0$, $m > -1$	$b(m+1)$	$b^2(m+1)$
Weibull	$\frac{1+m}{b} (x/b)^m \exp[-(x/b)^{1+m}]$, $m > -1$, $b > 0$	$b \Gamma(\frac{2+m}{1+m})$	$b^2 \left\{ \Gamma(\frac{3+m}{1+m}) - \left[\Gamma(\frac{2+m}{1+m}) \right]^2 \right\}$
Gaussian	$\frac{1}{\sigma_S \sqrt{2\pi}} \exp\left[-\frac{1}{2} \left(\frac{x-\mu_S}{\sigma_S}\right)^2\right]$, $\sigma_S > 0$	μ_S	σ_S^2
Poisson	$\frac{\lambda^{N_S-1}}{(N_S-1)!} \exp(-\lambda)$, $\lambda > 0$	λ	λ
Pareto	$\frac{\gamma}{m} \left(\frac{m}{x+1}\right)^{\gamma+1}$, $\gamma > 0$	$\gamma m / (\gamma - 1)$ ∞	$\gamma m^2 / [(\gamma - 2)(\gamma - 1)^2]$ ∞
		$\gamma > 1$ $\gamma \leq 1$	$\gamma > 2$ $\gamma \leq 2$

was identical, the position in reciprocal space of the $[00.(2h)]_{w \rightarrow h2}$ reflection would exactly coincide with the $[hhh]_{z \rightarrow c}$ reflection. However, the small difference in this interplanar spacing induces a slight offset of the zinc blende and wurtzite structure and the wurtzite zinc blende polytypism can be studied by measuring a region in reciprocal space containing the $[hhh]_{z \rightarrow c}$ and the $[00.(2h)]_{w \rightarrow h2}$ reflection. At the bottom right of Fig. 1, a graphical illustration of the zinc blende and wurtzite structure as it might occur inside a nanowire is depicted. Additional background information (including the mathematical relations for non-symmetric Bragg reflections) is given, for example, by Köhl (2014) and Biermanns (2012).

If we define the atomic form factors $f^\alpha(\mathbf{q})$ as the Fourier transform of the electron density of an atom of type α centred around the origin [*i.e.* $f^\alpha(\mathbf{q}) = \text{FT}_{\mathbf{x} \leftarrow \mathbf{q}}\{\rho_{\text{el}}^{(\alpha)}\}$], the Fourier transform of the electron density of a single wire w in the q_z direction ($\mathbf{q}_\perp = 0$) close to \mathbf{Q}_B is given by

$$\mathcal{F}_w^{(\text{SW})}(q_z, \mathbf{Q}_B) \propto \sum_{l=1}^{N_l} \tilde{\Omega}_w^{(l)} \exp(-iq_z z_{wl}) \times \sum_{\alpha \in \{\text{Ga, As}\}} f_\alpha(\mathbf{Q}_B) \exp(-iq_z \zeta_{wl\alpha}). \quad (18)$$

Here, z_{wl} is the beginning of layer j in wire w , *i.e.*

$$z_{w0} = 0, \quad z_{wl} \stackrel{l \geq 1}{=} \sum_{k=0}^{l-1} d_j^{(w)}, \quad (19)$$

where $d_j^{(w)}$ is the thickness of the GaAs layer j in wire w . $\zeta_{wl\alpha} = 0$ for $\alpha = \text{As}$ and $\zeta_{wl\alpha} = (3/4)d_j^{(w)}$ for $\alpha = \text{Ga}$. $\tilde{\Omega}_w^{(l)}$ is the in-plane cross section of layer j in wire w .

As long as radial growth is absent or only epitaxial in such a way that no tapering emerges, $\tilde{\Omega}_w$ is independent of j . If pronounced tapering is observed, it can be included in a straightforward manner by $\tilde{\Omega}_w^{(l)}$. For simplicity, we assume the absence of tapering in our result section, but we point out that the conclusions drawn from this special case are also valid for non-zero tapering.

Finally, we need to define how the layer spacings $d_j^{(w)}$ are obtained.

For that purpose, we compare the type of layer in the stacking sequence of layer $j - 1$ and $j + 1$: if both are equal, we locally have a wurtzite stacking and assign the value d_{WZ} to it. If the type of these two layers differs, we attribute d_{ZB} which we retrieve from the bulk value of cubic GaAs. For the ratio $d_{\text{WZ}}/d_{\text{ZB}}$, we employ 1.007 (Köhl *et al.*, 2015; Biermanns *et al.*, 2011; Biermanns, 2012).

In this model, we therefore neglect strain effects at the interface of the different polytypes. If, as a result of the statistical generation of the stacking sequence, higher polytypes (Johansson *et al.*, 2012) are contained in the stacking, their spacing scales linear with the hexagonality: a hexagonality of 0 corresponds to zinc blende, the $4H$ polytype to a hexagonality of 0.5 and wurtzite to 1.0. More advanced modelling of such strain effects can be easily incorporated, but this simple model is fully sufficient for the discussions in the results section.

With this information, formulas and definitions, we are able to calculate the scattering of a single nanowire.

Since we aim to extract results with high statistical significance, we need to probe a large number of nanowires. For this, we assume a large beam spot (for example, of the order of $1 \text{ mm} \times 1 \text{ mm}$). However, the coherence length for X-rays at current scattering beamlines at synchrotron facilities is typically of the order of micrometres, and, therefore, similar to typical nanowire densities ($1 \text{ wire}/\mu\text{m}^2$). Therefore, we assume that from the contributions from different wires the measured intensity distribution $\mathcal{I}(q_z, \mathbf{Q}_B)$ is obtained by an incoherent summation

$$\mathcal{I}(q_z, \mathbf{Q}_B) = \sum_{w=1}^{N_w} |\mathcal{F}_w^{(\text{SW})}(q_z, \mathbf{Q}_B)|^2. \quad (20)$$

Here, $N_w \gg 1$ is the number of wires encountered by the X-ray beam. Throughout the results section we set $N_w = 2500$ and employ an equidistant spacing of $2 \times 10^{-5} \text{ \AA}^{-1}$ for q_z in our simulations. In order to remove tiny residual fluctuations which we observe despite the huge number of wires $N_w = 2500$ in some cases (statistical distributions with high fluctuations), the result of our simulations smoothed by a running average with (maximum) 50 simulated points (*i.e.* points spanning a range 10^{-3} \AA^{-1}).

3. Results for the layer-by-layer modelling (Markov model)

We now turn to numerical results of our simulations for the Markov model (Fig. 4). Since this model has already been employed for interpretation of the first time-resolved *in situ* X-ray intensity profiles along the q_z direction close to the $[111]_c$ Bragg reflection (Schroth *et al.*, 2015), an extended analysis of this model and its comparison with other models for the distribution of the polytypes will now be presented.

In Fig. 4(a) we show the X-ray profiles for the same parameters as for the direct space illustration of the polytype distributions in Fig. 2. These profiles, and all other profiles depicted in this manuscript other than Fig. 7(a), are normalized to equal area for best comparison of their shapes, whereas the profiles depicted in Fig. 7(a) are normalized to a maximum of 1.

A qualitative discussion about the changes of these profiles as a function of the phase fractions and as a function of the phase purities at fixed phase fraction has already been given (Schroth *et al.*, 2015). We supplement this qualitative discussion here by the results depicted in Fig. 4(b) which contains the three lowest (central and normalized) moments (centre of mass, standard deviation and skewness) of the intensity distribution in reciprocal space close to the $[111]_c$ Bragg reflection of GaAs.

The centre of mass of our X-ray profiles is calculated as

$$\mu = \int_{1.90 \text{ \AA}^{-1}}^{1.9367 \text{ \AA}^{-1}} q_z \tilde{\mathcal{I}}(q_z) dq_z, \quad (21a)$$

the standard deviation as

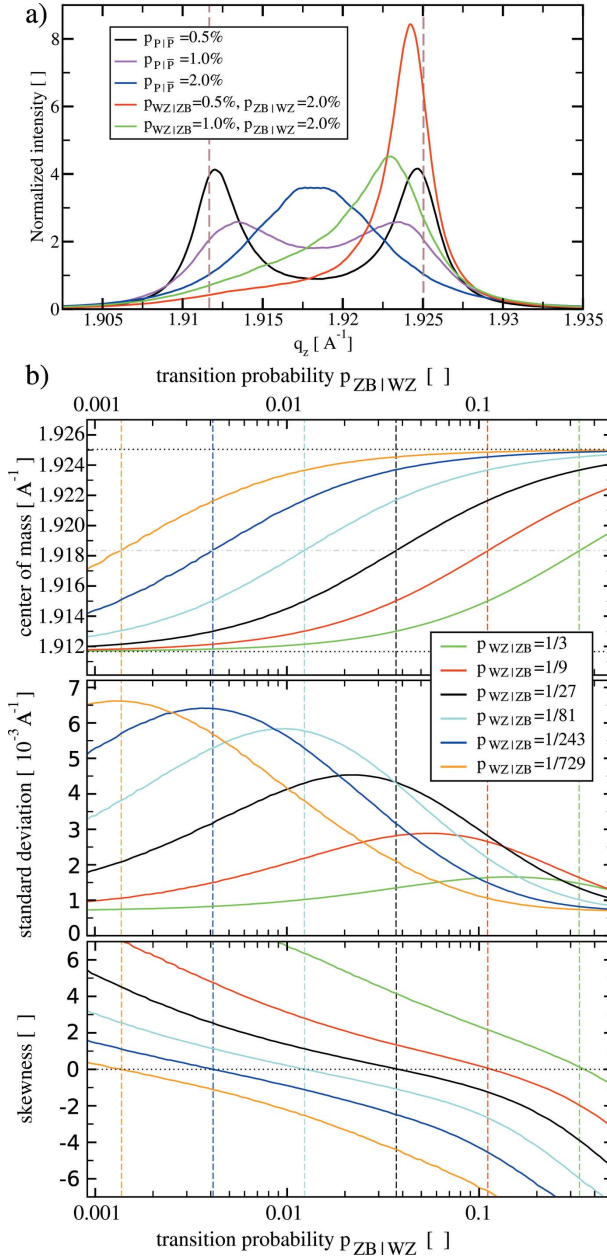


Figure 4 Characteristics and quantitative evaluation of the q_z intensity profile close to the $[111]_c$ Bragg reflection of GaAs. (a) Scattering profiles for the parameters underlying Fig. 2. (b) Centre of mass, standard deviation and skewness of the intensity profiles $\mathcal{I}(q_z)$ in the framework of the Markov model.

$$\sigma = \left[\int_{1.90 \text{\AA}^{-1}}^{1.9367 \text{\AA}^{-1}} (q_z - \mu)^2 \tilde{\mathcal{I}}(q_z) dq_z \right]^{1/2}, \quad (21b)$$

and, finally, the skewness as

$$s = \int_{1.90 \text{\AA}^{-1}}^{1.9367 \text{\AA}^{-1}} \left(\frac{q_z - \mu}{\sigma} \right)^3 \tilde{\mathcal{I}}(q_z) dq_z. \quad (21c)$$

Here, $\tilde{\mathcal{I}}$ is the normalized intensity

$$\tilde{\mathcal{I}}(q_z) = \mathcal{I}(q_z) / \left[\int_{1.90 \text{\AA}^{-1}}^{1.9367 \text{\AA}^{-1}} \mathcal{I}(q_z) dq_z \right]. \quad (22)$$

For symmetric conditions $p_{WZ|ZB} = p_{ZB|WZ}$, the skewness is equal to zero and the centre of mass is the average of the native zinc blende and wurtzite positions. Both the skewness and the centre of mass change monotonously. Contrarily, the width of the profiles shows a maximum for $p_{ZB|WZ} \gtrsim p_{WZ|ZB}$ and behaves non-monotonously. We point out that the maximum width is not obtained for strictly symmetric conditions $p_{WZ|ZB} = p_{ZB|WZ}$.

If we could estimate two of these moments, we could estimate the static transition probabilities $p_{WZ|ZB}$ and $p_{ZB|WZ}$ in the framework of the Markov model.

Since the skewness is a monotonous function of $p_{ZB|WZ}$, we can re-arrange these results and depict results for fixed skewness s . The result of this rearrangement is depicted in Fig. 5.

For a wide range of parameters the wurtzite fraction in the wires is a very flat function for given skewness s of the $[111]_c$ intensity profile [see Fig. 5(a)]. We emphasize that the skewness of a measured profile can be estimated without q_z calibration. However, we remind the reader that for proper

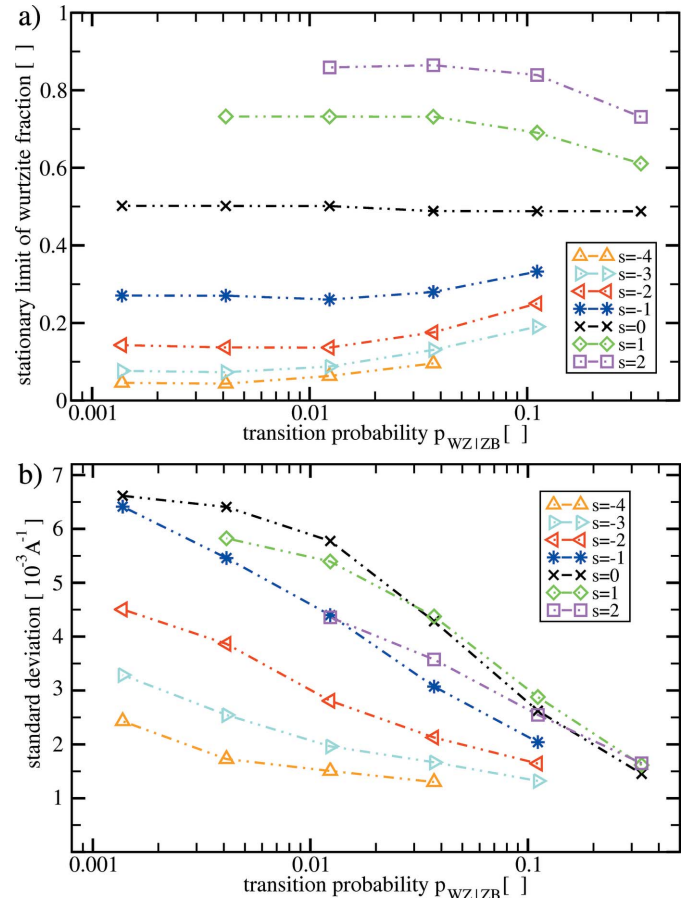


Figure 5 Rearrangement of the results given in Fig. 4(b): each depicted branch corresponds to a given constant skewness s . (a) Phase fraction of wurtzite for given skewness s as a function of the transition probability $p_{WZ|ZB}$. (b) Width of the X-ray profile for given skewness s as a function of the transition probability $p_{WZ|ZB}$.

interpretation of the experimental profile a correction for the contribution of parasitic growth to the scattering signal is required (Köhl *et al.*, 2015), and the resolution element must be either negligible or well known.

Knowledge of the width of the intensity profile (in addition to its skewness) is then sufficient to extract not only the phase fractions but also the values for the transition probabilities and, thus, the phase purities. The relation of the width of the profile with the transition probability $p_{ZB|WZ}$ can be found in Fig. 5(b). As expected, the width of the profile is decreasing with increasing transition probability $p_{ZB|WZ}$ for fixed skewness s .

4. Results for the segment-by-segment modelling

4.1. Generalizations of the Markov model: Gamma and Weibull distributions

After this in-depth exploration of the Markov model for the stacking sequences in the nanowires, it is interesting to investigate the effect of certain deviations from the Markov model on the q_z intensity profile close to the $[111]_c$ Bragg reflection of GaAs.

As we already discussed, the length distribution of the polytypic segments without stacking faults in the Markov model is given by the exponential distribution, equation (2), which is a special case of the Gamma distribution [see equation (11)] as well as of the Weibull distribution [see equation (11)]. Therefore, we discuss the results for these distributions first (see Fig. 6). For the special case $m = 0$ (continuous lines) we also give the corresponding transition probability p_{FP} of the Markov model. For simplicity, we restrict to symmetric conditions $p_{WZ|ZB} = p_{ZB|WZ}$, although all statements are valid also for non-equal transition probabilities.

We observe [see Fig. 6(a)] that neither an enhancement of short segments ($m < 0$) nor a reduction of short segments ($m > 0$) in comparison with the Markov model has strong influence on the shape of the intensity distribution. Even worse, all characteristic features are identical. For example, the profile for $m = 0$ and decay length $b = 140$ is essentially identical to the case $m = 1.0$ and $b = 100$. Consequently, such deviations in statistics of short segments could not be revealed by an observation of the intensity profile of the $[111]_c$ Bragg reflection of GaAs. For each deviation of the Markov model $m \neq 0$ and $b = 100$ we also depict the result for the Markov model that corresponds to the same expectation value as the non-Markovian case. For all three cases the results for the corresponding cases differ. And in all three cases the change in the profile in the Markov model $m = 0$ with the expectation value compared with $m = 0$ and $b = 100$ is greater than if the change in the expectation value originates in a change in the statistics of short segments (*i.e.* $m \neq 0$). Therefore, the shape of the profile does not even uniquely map to the expectation value of the polytype length distribution. From these results we see that the decay lengths b of both polytypes have strongest influence on the intensity profile. Thus, if deviations of the Markov model are expected for small polytypic segments, the interpretation and discussion of the respective

X-ray profiles should be based on these decay lengths b instead of the expectation values of the length distributions of the polytype segments. Otherwise, the interpretation entails large systematic uncertainties.

Whereas the Gamma distribution mainly introduces a deviation from the Markov model for short segments, the Weibull distribution also mimics strong changes in the statistics of long segments. Despite these even stronger deviations, the X-ray profile is still not unique [see, for example, the two cases ($m = 0.0, b = 333$ layer) and ($m = -0.4, b = 100$ layer) in Fig. 6(b)]. If we compare the three cases with the expectation value $\mu = 100$ (continuous lines), the shape of the intensity profile changes tremendously with the parameter m , although the characteristic features remain identical to the Markov model. For each value m , the Markov case for decay length $b = 100$ has also been depicted. Clearly, the influence of the decay lengths b is minor as compared with the parameter m .

Therefore, we could identify the following hierarchy for the influence on the shape of the X-ray profile: most important is the decay of the length distribution for long segments where the exponents of the exponentials are more important than the decay lengths. Contrarily, deviations for short segments have only small influence. Unique identification of the X-ray profile is only possible if two out of the three features ‘long-length decay behaviour’, decay length scale and ‘short length deviations’ are known. For the Markov model, the only free parameters are the decay length b_p and unique extraction of this parameter for both polytype is possible.

A common feature of the exponential distribution and the Gamma as well as the Weibull distribution is large intrinsic fluctuations that scale with the decay lengths. Specifically, we have the mean values

$$\mu_G = b(m + 1), \quad (23a)$$

$$\mu_W = b \Gamma\left(\frac{2 + m}{1 + m}\right), \quad (23b)$$

and standard deviations

$$\sigma_G = b(m + 1)^{1/2}, \quad (24a)$$

$$\sigma_W = b \left\{ \Gamma\left(\frac{3 + m}{1 + m}\right) - \left[\Gamma\left(\frac{2 + m}{1 + m}\right) \right]^2 \right\}^{1/2} \quad (24b)$$

for the Gamma and Weibull distribution, respectively. It is this huge standard deviation σ which is of the same order as the mean value μ that defines the characteristics of the X-ray profiles.

4.2. Towards super-cell structures: the influence of fluctuations of the polytype segment lengths

In order to study the influence of these fluctuations, we now decouple the mean and standard deviation and model the phase segment length distribution by considering a Gaussian distribution [see Fig. 7(a)]. As long as the standard deviation is of comparable order of magnitude as the mean value, the X-ray profile resembles the same characteristic features as for the Gamma and Weibull distributions. Once the standard

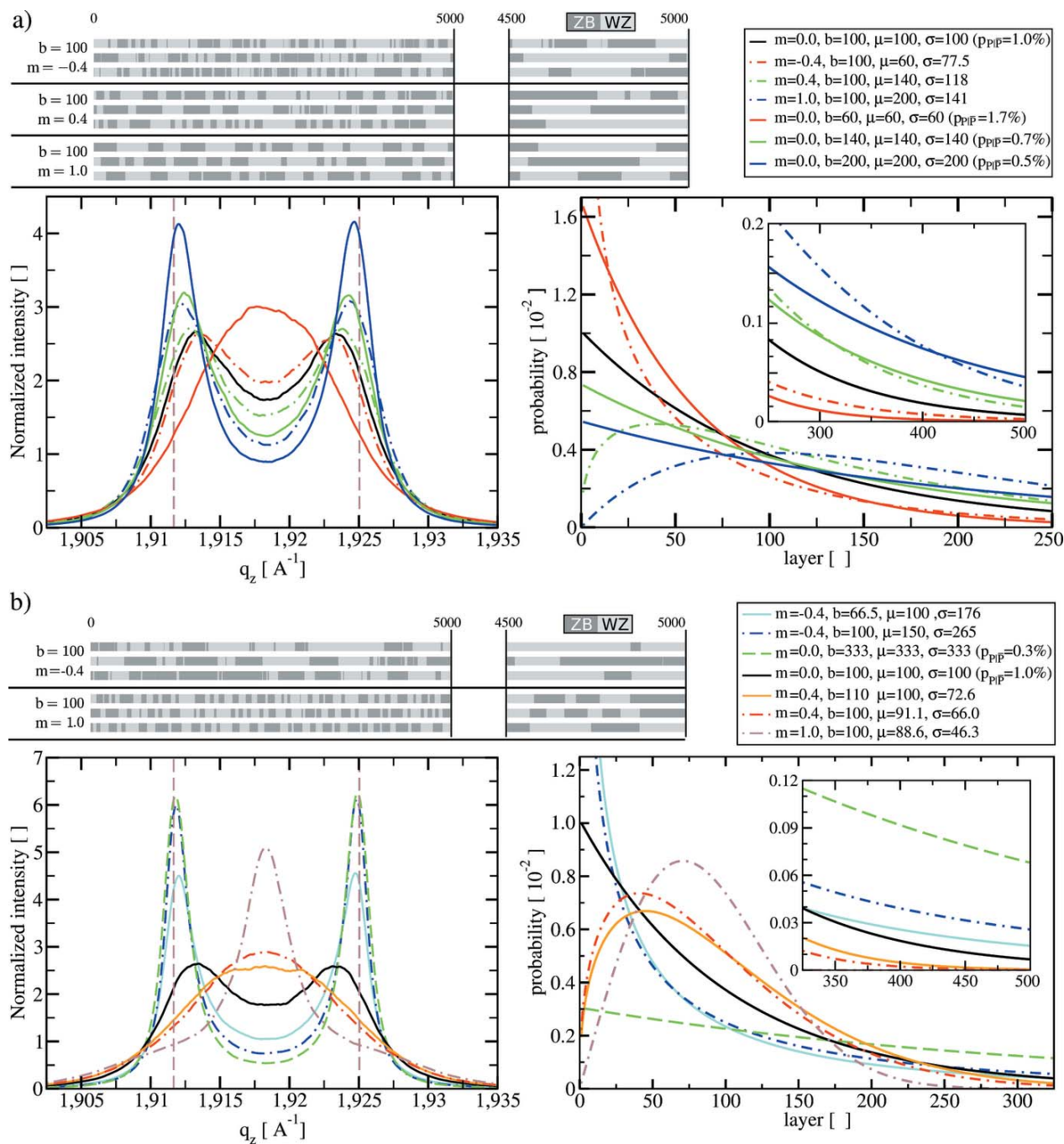


Figure 6

Examples for the X-ray intensity profiles for length distributions of each polytype given by (a) a Gamma or (b) a Weibull distribution which both contain the exponential distribution (Markov model) as special case. μ refers to the expectation value and σ to the standard deviation of the respective distributions. The parameters b and m are defined in equations (11) and (12), respectively. For illustration, we also depicted the respective probability density functions as well as several realisations of the segment distribution inside the nanowires.

deviation is significantly smaller than the mean value, the characteristic features change dramatically. Instead of two broad overlapping peaks, beating phenomena are observed as a consequence of the high correlations in the phase segment distribution in direct space. This limit of high correlations corresponds to super-lattices in phase distribution in direct space. If we go even one step further, and model the phase distribution in direct space by a Poisson distribution (standard deviation scales only like the square root of the mean value),

we also observe such beating phenomena [see Fig. 7(b)]. From the spacing of two sub-peaks from such a beating signal, we can retrieve the sum of the mean values of the Poisson distribution of both polytypes, whereas the absolute q_z positions reveals the relative fractions of the polytypes. In summary, we can deduce from the results in Fig. 7 that X-ray diffraction measurements of the vicinity of the $[111]_c$ Bragg reflection are highly suited for studying the quality of alternating zinc blende wurtzite super-lattices.

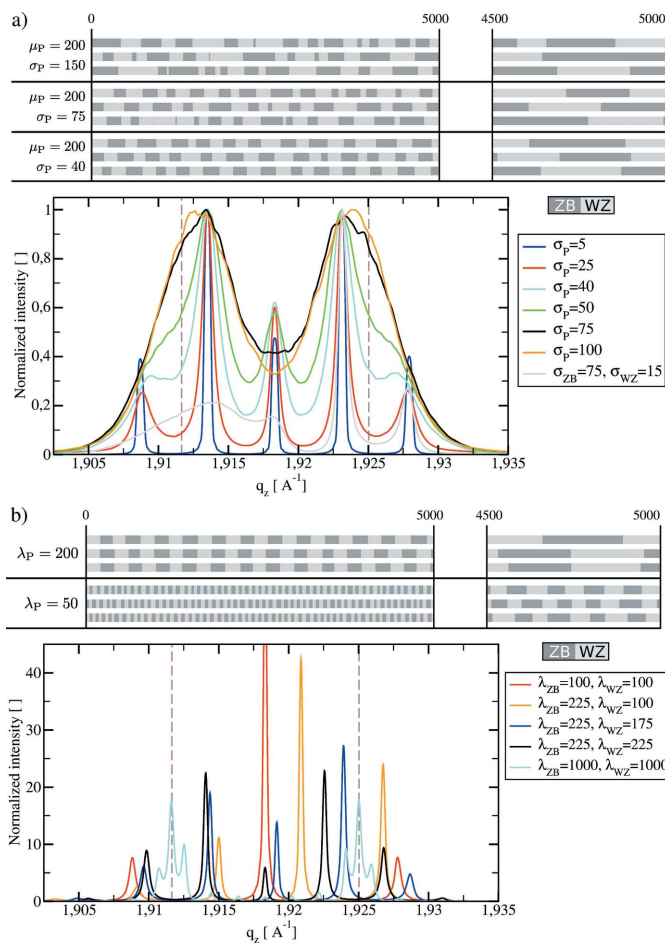


Figure 7
Influence of fluctuations on the shape of the X-ray profile close to the $[111]_c$ Bragg reflection of GaAs: (a) Gaussian distribution ($\mu_p = 200$ layer) and (b) Poisson distribution. Parameters are defined in equations (13) and (14), respectively.

4.3. Polynomial polytype segment length distributions

Up to now, the decay of the phase segment distribution was related to the exponential function. If we instead consider a power law decay [‘Pareto distribution’, see equation (15)] for the probability for long defect-free polytype segments in the stacking sequence in the $(111)_c$ growth direction, we also observe an interesting shape of the intensity profile close to the $[111]_c$ GaAs Bragg reflection (see Fig. 8): for exponents $\gamma \lesssim 1.5$ we observe pronounced and very sharp peaks at the native positions of both polytypes. In contrast to behaviour for the Gamma and Weibull distributions, these peaks do not drift towards each other with decreasing phase purity (*i.e.* increasing parameter γ).

For $1.0 \lesssim \gamma \lesssim 1.5$, a third, broader, peak in between the native positions of the polytypes emerges. Its centre drifts for asymmetric conditions $p_{WZ|ZB} \neq p_{ZB|WZ}$, whereas the peaks at the native positions only change the weight (see the two examples $\gamma_{ZB} = 1.3, \gamma_{WZ} = 1.0$ and $\gamma_{ZB} = 1.3, \gamma_{WZ} = 1.8$).

These peculiar features stem from the combination of the slowly decaying tails of the length distribution for the polytype segments and the large probability for very small segments.

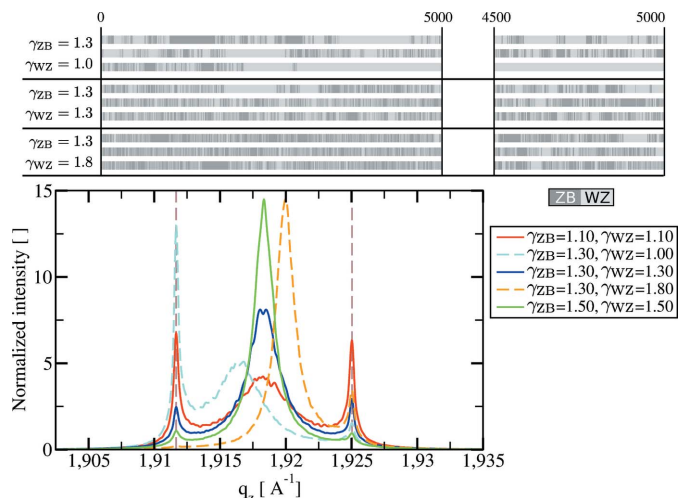


Figure 8
Examples for the X-ray intensity profiles for a length distributions of each polytype given by a Pareto distribution.

Such a central peak, which drifts with the asymmetry, has already been observed in the Markov model for highly faulty wires [see Fig. 4(a)]. In contrast, two sharp peaks at the native positions of both polytypes have been observed for nanowires with very high phase purity. A power law distribution mixes these two cases for a certain range of parameters. For large decay parameter $\gamma \gtrsim 1.5$, we essentially observe only the limit of highly faulty wires. For small decay parameter $\gamma \lesssim 1.0$, the long defect-free polytype segments from the slowly decaying tails of the Pareto distribution determine the shape of the X-ray signal. We point out that power law distributions are scale-free, and, consequently, the zoom of the direct space realisations in Fig. 8 resembles very closely the features on the larger scale.

In summary, we demonstrated in this section the importance of fluctuations and, strongly related, correlations in the phase distributions in direct space. On the one hand, we discussed the non-uniqueness of the X-ray q_z intensity profile for distributions with high fluctuations if more than one parameter of the phase segment distribution is not known. However, we could still rank the importance of deviations from the Markov model for short- or for long-phase segments. On the other hand, we investigated the transition of the X-ray signal if these fluctuations are decreased more and more. Finally, we also investigated the consequences of the absence of an exponential decrease for the probability to observe a long defect-free polytype segment.

4.4. 4H occurrence beyond its statistical expectation

Up to this point, other (higher-order) polytypes than zinc blende or wurtzite are only observed according to their combinatorial probability (Johansson *et al.*, 2012). However, an enhancement of specific polytypes, most importantly the 4H polytype, should be investigated (Dubrovskii & Sibirev, 2008; Johansson *et al.*, 2012; Panse *et al.*, 2011).

Since the 4H structures are constituted by a stacking of type ABCB, we enhance the 4H wurtzite structures in the nano-

wires stacking if we specifically increase the probability for a phase segment with length 1. We point out that this is different from enhancing short segment lengths in the case of Gamma or Weibull distributions, since the enhancement of the 4H is not equally selective.

Consequently, a model for the enhancement of the 4H is the length distribution

$$p_{P,4H+}^{(\alpha)}(j) = (1 - \alpha_p) p_P^{(\text{loc})}(j) + \alpha_p p_{1+}(j) \quad (25a)$$

$$\stackrel{\text{Eq. 2}}{=} (1 - \alpha_p) \frac{\exp(-j/b_P)}{b_P} \Theta(j) + \alpha_p \delta_{1j} \quad (25b)$$

for the zinc blende and wurtzite polytype P. Here, the parameter $\alpha_p \in [0, 1]$ and δ_{ij} is the Kronecker delta. The limit $\alpha = 0$ corresponds to the original Markov model. The limit $\alpha = 1$ results in pure 4H nanowires.

Within this model, the length distribution of the 4H segments is well approximated by the exponential distribution

$$p_{4H}(j) = \frac{\exp(-j/b_{4H})}{b_{4H}} \Theta(j) \quad (26)$$

with decay length

$$b_{4H} = -2 / \log \left[\left(\frac{1}{b_{ZB}} + \alpha_{ZB} \frac{b_{ZB} - 1}{b_{ZB}} \right) \left(\frac{1}{b_{WZ}} + \alpha_{WZ} \frac{b_{WZ} - 1}{b_{WZ}} \right) \right]. \quad (27)$$

For the decay length b_{4H} to be significantly larger than 1, either both parameters b_P must be of the order of unity or the parameters α_P must be both very close to 1.

It is important to understand that, for values of α_p very close to 1, almost all newly generated segments are only one layer thick. In contrast, every rare event $(1 - \alpha_p)$ typically adds a large number of layers to the stacking.

The condition $b \equiv b_P = b_{4H}$ is fulfilled for $\alpha \equiv \alpha_p$ if

$$\alpha = \frac{1}{b - 1} \left[b \exp\left(\frac{-1}{b}\right) - 1 \right] \stackrel{b \gg 1}{\approx} 1 - \frac{1}{b}. \quad (28)$$

For this order of magnitude of α_p , the amount and purity of the 4H polytype becomes comparable with wurtzite and zinc blende.

Typical results for this model are depicted Fig. 9. The 4H polytype shows up as a third sub-peak which ‘interacts’ with the sub-peaks of zinc blende and wurtzite. The same observations as for the Markov model (see Fig. 4) apply, but now for three sub-peaks. For very pure wires, (up to) three essentially independent sub-peaks can be observed [$1 - \alpha_p \approx (1/b_P) \ll 1\%$, continuous lines in Fig. 9]. For decreasing phase purity, the peaks overlap and plateaus emerge. If only very short 4H segments exist in the nanowires, the middle peak becomes so broad that essentially only the wurtzite and zinc blende peaks are observable. For $1 - \alpha \gg (1/b)$, the 4H is barely detectable by studying the $[111]_c$ Bragg reflection of GaAs. This case of three split peaks resembles the profiles for the Pareto distributions (see Fig. 8). Consequently, misinterpretations are possible if one is not aware of these non-uniquenesses.

For $1 - \alpha_p \approx (1/b_P) \gtrsim 1\%$, the 4H enhanced signal shows similar characteristics as the signal in the Markov model (see

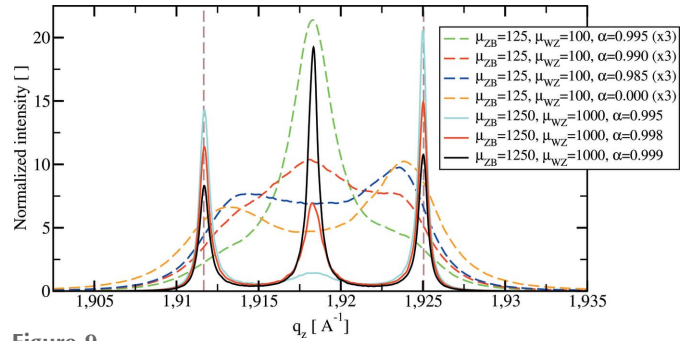


Figure 9

Examples for the X-ray q_z intensity profiles for an occurrence of the 4H polytype which is increased above its combinatorial likelihood [see equation (25)]. The less pure structures (dashed lines) have been normalized to three times the area of the structures with higher phase purity for better visibility.

dashed lines in Fig. 9) and the segment-by-segment growth model based on Gamma and Weibull distributions. Consequently, misinterpretations are also possible for this range of values for the parameter α_p .

4.5. Relations between the $[333]_c$ and $[111]_c$ Bragg reflection

We now provide a short excursion on the relation of the $[111]_c$ and $[333]_c$ reflection (and higher-order symmetric reflections).

Up to now, we solely focused on the $[111]_c$ GaAs Bragg reflection. These profiles are related to the respective profiles of the $[333]_c$ Bragg reflection by a rescaling of the transition probabilities and the q_z axis: within the Markov model, the q_z profiles of the $[333]_c$ reflection with transition probabilities $p_{P\bar{P}P}$ are equal to the profiles of the $[111]_c$ reflection with transition probabilities $p_{\bar{P}P\bar{P}}/3$ evaluated at $q_z/3$. This behaviour is illustrated in Fig. 10. In this figure the profiles calculated directly are equal to those obtained by the scaling relation. For comparison, the shape of the $[111]_c$ and $[333]_c$ profiles for identical transition probabilities $p_{P\bar{P}P}$ is depicted in this figure. As expected from the scaling relation, the peaks are well separated for transition probabilities three times larger than for the $[111]_c$ reflection. Therefore, information on nanowires with high transition probabilities $p_{P\bar{P}P}$ is extracted more easily from the shape of the $[333]_c$ Bragg reflection than from the $[111]_c$ Bragg reflection.

The origin of this scaling relation can be understood from the phase segment length distribution which is given in equation (2): up to the normalization, the functional dependence is fully determined by the ratio n/b_P . The three times larger value of q_z of the $[333]_c$ reflection can be achieved by variation of the scattering angles towards larger angles or by reduction of the X-ray wavelength or combinations thereof. The scaling behaviour is most easily understood if we absorb the full multiplicative factor of three in a decrease of the X-ray wavelength of three while maintaining identical scattering angles. As long as the discreteness of the atomic scale is not relevant for the phase correlations of the scattered intensity (which is taken care of by the centre of the Bragg peak and thus no longer relevant for the behaviour in its close vicinity),

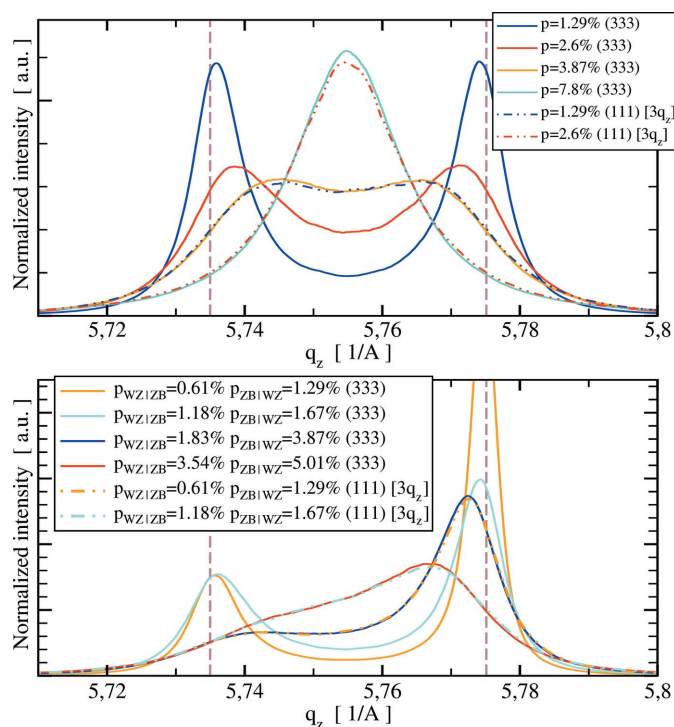


Figure 10
Illustration of the relation between the $[111]_c$ and $[333]_c$ reflection for $p = P_{ZB|WZ} = P_{WZ|ZB}$ (upper figure) and $P_{ZB|WZ} \neq P_{WZ|ZB}$ (lower figure).

we effectively reduce the n in equation (2) which produces the same phase shift by a factor of three. If we compensate for this reduction by a simultaneous rescaling of b_p by a factor of three, *i.e.* increasing $p_{\text{PIP}} = b_p^{-1}$ in the Markov model by a factor of three, the interference pattern of a single nanowire does not change and, thus, the incoherent average does neither.

From this discussion, it is clear that the same reasoning also applies to Gamma and Weibull distributions which are also a function of the ratio n/b_p and neither n nor b_p is coupled to the additional parameter of these distributions separately. Thus, a rescaling of b_p by a factor of three precisely produces the shape of the corresponding $[333]_c$ reflection. Hence, deviations from the Markov model for the stacking in nanowires towards Gamma- or Weibull-like behaviour can even *not* be extracted based on the combination of measurements of the $[111]_c$ and $[333]_c$ reflection.

5. Conclusion

In summary, we demonstrated that great care is required in order to avoid misinterpretations of X-ray measurements of the $[111]_c$ Bragg reflection of polytypic nanowires.

Depending on the statistical properties of the distribution of the polytypes, a large variety of characteristic features is observed, ranging from beating phenomena in highly correlated systems such as super-lattice structures over three-peak behaviour in the case of length distributions decaying as a power law or enhanced occurrence of the $4H$ polytype to single-peak signals in the case of highly disordered nanowires.

However, despite the huge variety of characteristic features, the profile shape of the q_z profile of the $[111]_c$ Bragg reflection contains also a large number of ambiguities, most notably in the case of polytype distributions with large fluctuations of the length of each polytypic segment. A particularly important special case of the previous statement are Weibull- and Gamma-distributions for the lengths of a faultless polytype segment with parameter values resulting in distributions similar to an exponential distribution: the q_z profile close to the $[111]_c$ reflection requires a theoretical model for stacking in the nanowires which fixes all but one (independent) parameter.

In the case of a Markov model, the decay lengths, which equal the expectation value as well as the standard deviation of this distribution, (or transition probabilities) may be taken as this parameter. Moreover, the skewness of the measured signal already reveals the phase fractions of the polytypes. If additionally the width of the signal is taken into account, also the phase purities of the polytypes can be estimated easily.

High-quality super-lattices can easily be detected with X-ray diffraction experiments over a huge range of phase purities due to the characteristic beating phenomena in the X-ray profile. Contrarily, detection of an enhanced occurrence of the $4H$ polytype requires very pure polytype segments.

Due to the scaling relation between the profiles near the $[111]_c$ and $[333]_c$ reflection, measurements of the $[333]_c$ reflection extend the range of applicability to nanowires with three times lower phase purity. However, sufficiently high X-ray flux and energy as well as an adequate measurement setup are needed which is challenging in the case of time-resolved *in situ* X-ray experiments. Consequently, measuring a series of reflections on the asymmetric crystal truncation rod such as the reflections $[220]_c$ - $[10.3]_h$ - $[311]_c$ is often a better choice than the $[333]_c$ reflection *if* the experimental setup is capable of such measurements (for example, this series of reflections of a $[111]_c$ -oriented substrate can be measured at an X-ray energy of 15 keV by performing a rotation of the sample around its normal by a few degrees at a *fixed* incidence angle of 15.5° , while a current two-dimensional detector is located at a *fixed* position during this scan (Köhl, 2014).

We are convinced that future advances in the microscopic modelling of the growth dynamics of polytypic nanowires will remedy most of these ambiguities in the interpretation of the X-ray profiles of an ensemble of polytypic nanowires (by reducing the number of degrees of freedom in the models). Therefore, we believe that X-ray investigations of polytypic nanowires will become more and more important for verification and optimization of the growth of an ensemble of nanowires.

References

- Adams, D. E., Martin, L. S., Seaberg, M. D., Gardner, D. F., Kapteyn, H. C. & Murnane, M. M. (2012). *Opt. Express*, **20**, 24778–24790.
- Algra, R. E., Verheijen, M. A., Borgström, M. T., Feiner, L.-F., Immink, G., van Enkevort, W. J. P., Vlieg, E. & Bakkers, E. P. A. M. (2008). *Nature (London)*, **456**, 369–372.
- Bao, J., Bell, D. C., Capasso, F., Wagner, J. B., Mårtensson, T., Trägårdh, J. & Samuelson, L. (2008). *Nano Lett.* **8**, 836–841.

- Biermanns, A. (2012). Dissertation. Universität Siegen, Germany.
- Biermanns, A., Breuer, S., Davydok, A., Geelhaar, L. & Pietsch, U. (2011). *Phys. Status Solidi RRL*, **5**, 156–158.
- Biermanns, A., Davydok, A., Paetzelt, H., Diaz, A., Gottschalch, V., Metzger, T. H. & Pietsch, U. (2009). *J. Synchrotron Rad.* **16**, 796–802.
- Biermanns, A., Dimakis, E., Davydok, A., Sasaki, T., Geelhaar, L., Takahasi, M. & Pietsch, U. (2014). *Nano Lett.* **14**, 6878–6883.
- Cahangirov, S. & Ciraci, S. (2009). *Phys. Rev. B*, **79**, 165118.
- Caroff, P., Bolinsson, J. & Johansson, J. (2011). *Quantum Electron.* **17**, 829–846.
- Chushkin, Y. & Zontone, F. (2013). *J. Appl. Cryst.* **46**, 319–323.
- Dick, K. A., Caroff, P., Bolinsson, J., Messing, M. E., Johansson, J., Deppert, K., Wallenberg, L. R. & Samuelson, L. (2010). *Semicond. Sci. Technol.* **25**, 024009.
- Dubrovskii, V. G., Consonni, V., Geelhaar, L., Trampert, A. & Riechert, H. (2012). *Appl. Phys. Lett.* **100**, 153101.
- Dubrovskii, V. G. & Sibirev, N. V. (2008). *Phys. Rev. B*, **77**, 035414.
- Gamalski, A. D., Ducati, C. & Hofmann, S. (2011). *J. Phys. Chem. C*, **115**, 4413–4417.
- Gamalski, A. D., Tersoff, J., Sharma, R., Ducati, C. & Hofmann, S. (2012). *Phys. Rev. Lett.* **108**, 255702.
- Glas, F., Harmand, J.-C. & Patriarche, G. (2007). *Phys. Rev. Lett.* **99**, 146101.
- Heiss, M., Conesa-Boj, S., Ren, J., Tseng, H.-H., Gali, A., Rudolph, A., Uccelli, E., Peiró, F., Morante, J. R., Schuh, D., Reiger, E., Kaxiras, E., Arbiol, J. & Fontcuberta i Morral, A. (2011). *Phys. Rev. B*, **83**, 045303.
- Hjort, M., Lehmann, S., Knutsson, J., Timm, R., Jacobsson, D., Lundgren, E., Dick, K. & Mikkelsen, A. (2013). *Nano Lett.* **13**, 4492–4498.
- Johansson, J., Bolinsson, J., Ek, M., Caroff, P. & Dick, K. A. (2012). *ACS Nano*, **6**, 6142–6149.
- Johansson, J., Karlsson, L. S., Dick, K. A., Bolinsson, J., Wacaser, B. A., Deppert, K. & Samuelson, L. (2009). *Cryst. Growth Des.* **9**, 766–773.
- Johansson, J., Karlsson, L. S., Patrik, T., Svensson, C., Mårtensson, T., Wacaser, B. A., Deppert, K., Samuelson, L. & Seifert, W. (2006). *Nat. Mater.* **5**, 574–580.
- Joyce, H. J., Wong-Leung, J., Gao, Q., Tan, H. H. & Jagadish, C. (2010). *Nano Lett.* **10**, 908–915.
- Kaufholz, M., Krause, B., Kotapati, S., Köhl, M., Mantilla, M. F., Stüber, M., Ulrich, S., Schneider, R., Gerthsen, D. & Baumbach, T. (2015). *J. Synchrotron Rad.* **22**, 76–85.
- Köhl, M. (2014). Dissertation. Karlsruhe Institute of Technology, Karlsruhe, Germany.
- Köhl, M., Minkevich, A. A. & Baumbach, T. (2012). *Opt. Express*, **20**, 17093–17106.
- Köhl, M., Schroth, P., Minkevich, A. A. & Baumbach, T. (2013). *Opt. Express*, **21**, 27734–27749.
- Köhl, M., Schroth, P., Minkevich, A. A., Hornung, J.-W., Dimakis, E., Somaschini, C., Geelhaar, L., Aschenbrenner, T., Lazarev, S., Grigoriev, D., Pietsch, U. & Baumbach, T. (2015). *J. Synchrotron Rad.* **22**, 67–75.
- Kriegner, D., Panse, C., Mandl, B., Dick, K. A., Keplinger, M., Persson, J. M., Caroff, P., Ercolani, D., Sorba, L., Bechstedt, F., Stangl, J. & Bauer, G. (2011). *Nano Lett.* **11**, 1483–1489.
- Krogstrup, P., Hannibal Madsen, M., Hu, W., Kozu, M., Nakata, Y., Nygård, J., Takahasi, M. & Feidenhans'l, R. (2012). *Appl. Phys. Lett.* **100**, 093103.
- Mandl, B., Stangl, J., Mårtensson, T., Mikkelsen, A., Eriksson, J., Karlsson, L. S., Bauer, G., Samuelson, L. & Seifert, W. (2006). *Nano Lett.* **6**, 1817–1821.
- Marchesini, S. (2007a). *J. Opt. Soc. Am. A*, **24**, 3289–3296.
- Marchesini, S. (2007b). *Rev. Sci. Instrum.* **78**, 011301.
- Mariager, S. O., Lauridsen, S. L., Sørensen, C. B., Dohn, A., Willmott, P. R., Nygård, J. & Feidenhans'l, R. (2010). *Nanotechnology*, **21**, 115603.
- Minkevich, A. A., Köhl, M., Escoubas, S., Thomas, O. & Baumbach, T. (2014). *J. Synchrotron Rad.* **21**, 774–783.
- Moseler, M., Cervantes-Sodi, F., Hofmann, S., Csányi, G. & Ferrari, A. C. (2010). *ACS Nano*, **4**, 7587–7595.
- Panse, C., Kriegner, D. & Bechstedt, F. (2011). *Phys. Rev. B*, **84**, 075217.
- Rodriguez, J. A., Xu, R., Chen, C.-C., Zou, Y. & Miao, J. (2013). *J. Appl. Cryst.* **46**, 312–318.
- Schroth, P., Köhl, M., Hornung, J.-W., Dimakis, E., Somaschini, C., Geelhaar, L., Biermanns, A., Bauer, S., Lazarev, S., Pietsch, U. & Baumbach, T. (2015). *Phys. Rev. Lett.* **114**, 055504.
- Schroth, P., Slobodskyy, T., Grigoriev, D., Minkevich, A., Riote, M., Lazarev, S., Fohtung, E., Hu, D., Schaadt, D. & Baumbach, T. (2012). *Mater. Sci. Eng. B*, **177**, 721–724.
- Sebastian, M. T. & Krishna, P. (1987). *Cryst. Res. Technol.* **22**, 929–941.
- Slobodskyy, T., Schroth, P., Grigoriev, D., Minkevich, A. A., Hu, D. Z., Schaadt, D. M. & Baumbach, T. (2012). *Rev. Sci. Instrum.* **83**, 105112.
- Spirkoska, D., Arbiol, J., Gustafsson, A., Conesa-Boj, S., Glas, F., Zardo, I., Heigoldt, M., Gass, M. H., Bleloch, A. L., Estrade, S., Kaniber, M., Rossler, J., Peiro, F., Morante, J. R., Abstreiter, G., Samuelson, L. & Fontcuberta i Morral, A. (2009). *Phys. Rev. B*, **80**, 245325.
- Takahashi, K. & Morizumi, T. (1966). *Jpn. J. Appl. Phys.* **5**, 657–662.
- Tchernycheva, M., Harmand, J. C., Patriarche, G., Travers, L. & Cirilin, G. E. (2006). *Nanotechnology*, **17**, 4025–4030.
- Trahan, R. & Hyland, D. (2013). *Appl. Opt.* **52**, 3031–3037.
- Yeh, C.-Y., Lu, Z. W., Froyen, S. & Zunger, A. (1992). *Phys. Rev. B*, **46**, 10086–10097.
- Zheng, H., Wang, J., Huang, J. Y., Wang, J., Zhang, Z. & Mao, S. X. (2013). *Nano Lett.* **13**, 6023–6027.